## Title

Correlated spectroscopic imaging of calf muscle in three spatial dimensions using group sparse reconstruction of undersampled single and multichannel data



## Journal

Magnetic Resonance in Medicine, 74(5)

## ISSN

0740-3194

## Authors

Wilson, Neil E
Burns, Brian L
Iqbal, Zohaib
et al.

## Publication Date

2015-11-01

## DOI

10.1002/mrm.25988

Peer reviewed

RAPID COMMUNICATION

Magnetic Resonance in Medicine 00:00–00 (2015)

# Correlated Spectroscopic Imaging of Calf Muscle in Three Spatial Dimensions Using Group Sparse Reconstruction of Undersampled Single and Multichannel Data

Neil E. Wilson, Brian L. Burns, Zohaib Iqbal, and M. Albert Thomas*

**Purpose:** To implement a 5D (three spatial + two spectral) correlated spectroscopic imaging sequence for application to human calf.

**Theory and Methods:** Nonuniform sampling was applied across the two phase encoded dimensions and the indirect spectral dimension of an echo planar-correlated spectroscopic imaging sequence. Reconstruction was applied that minimized the group sparse mixed $\ell_{2,1}$-norm of the data. Multichannel data were compressed using a sensitivity map-based approach with a spatially dependent transform matrix and utilized the self-sparsity of the individual coil images to simplify the reconstruction.

**Results:** Single channel data with 8× and 16× undersampling are shown in the calf of a diabetic patient. A 15-channel scan with 12× undersampling of a healthy volunteer was reconstructed using 5 virtual channels and compared to a fully sampled single slice scan. Group sparse reconstruction faithfully reconstructs the lipid cross peaks much better than $\ell_1$ minimization.

**Conclusion:** COSY spectra can be acquired over a 3D spatial volume with scan time under 15 min using echo planar readout with highly undersampled data and group sparse reconstruction. **Magn Reson Med 000:000–000, 2015. © 2015 Wiley Periodicals, Inc.**

**Key words:** EP-COSI; compressed sensing; nonuniform sampling; group sparsity; calf muscle; 3D spectroscopic imaging

## INTRODUCTION

Using the theory proposed by Jeener in 1971, Ernst and coworkers showed the first two-dimensional (2D) NMR spectra acquired using correlated spectroscopy (COSY) (1). A COSY spectrum is characterized by the presence of cross-peak multiplets indicating scalar coupling between protons and is achieved following the application of a 90° coherence transfer pulse to single quantum coherences and incrementing the echo time. Due to its relative simplicity, COSY was also one of the first 2D spectroscopy sequences successfully applied in vivo (2,3). While the spectral resolution in vivo is T2 limited and not high enough to fully resolve the individual peaks that comprise each cross peak multiplet, the overall cross peaks showcase the clear presence of coupled partners and where those partners resonate. Compared to single-dimensional (1D) spectra, COSY spectra are less dense with improved spectral dispersion. In skeletal muscle, COSY has been used to separately quantify the saturated and unsaturated fatty acid contributions to the intramyocellular and extramyocellular lipid pools (IMCL/EMCL), allowing more reliable calculation of the unsaturation index (4).

However, applications of COSY as a single voxel technique are greatly limited by the lack of coverage and the large voxel size. Spectroscopic imaging (SI) or chemical shift imaging (5) solves these problems while acquiring spectra from multiple locations simultaneously. Standard chemical shift imaging techniques use phase-encoding in each spatial direction and offer no improvement in scan time efficiency compared to single voxel techniques, making their combination with COSY prohibitively long for applications to humans (6). By interleaving the acquisition of an entire k-space line with the temporal or spectral information in a single excitation, an echo planar readout (7) can reduce the scan time by at least an order of magnitude. The remaining spatial dimension(s) are phase encoded (8).

Recently, COSY has been combined with an echo planar readout for correlated SI (EP-COSI) in rat brain (9) and in humans (10,11). These sequences have been limited in coverage to a single slice because of the scan times required to incrementally acquire a phase-encoded spatial direction ($k_y$) and the indirect spectral dimension ($t_1$). A fully sampled 3D volume scan would take hours even with the echo planar readout.

Nonuniform undersampling (NUS) with compressed sensing (CS) reconstruction has been used to accelerate the acquisition of these single-slice-correlated SI sequences by subsampling the plane spanned by the phase-encoded direction ($k_y$) and $t_1$ (12). Here we extend those techniques to subsample and reconstruct the volume spanned by two phase-encoded directions ($k_y$ and $k_z$) and $t_1$ by utilizing prior knowledge that the COSY spectrum is

Department of Radiological Sciences, University of California Los Angeles, Los Angeles, California, USA.

Grant sponsor: NIH/NIDDK; Grant number: 5R01DK090406.

*Correspondence to: M. Albert Thomas, Ph.D., Department of Radiological Sciences, University of California Los Angeles, Los Angeles, California, USA. E-mail: athomas@mednet.ucla.edu, Twitter: @mathomas95.

Received 31 March 2015; revised 23 August 2015; accepted 24 August 2015

DOI 10.1002/mrm.25988

Published online 00 Month 2015 in Wiley Online Library (wileyonlinelibrary.com).

self-sparse (i.e. the 2D spectra are composed of relatively few nonzero peaks surrounded by low-level noise). We also utilize the broadness of the peaks in vivo to improve the reconstruction by grouping coefficients that are in close proximity in the spectral plane. Qualitative comparison is performed between a mixed-norm group sparse (GS) reconstruction and a typical CS $\ell_1$-norm reconstruction using different undersampling factors with single channel and multichannel data. Reconstructions of prospectively undersampled whole calf correlated SI data with three spatial and two spectral dimensions are compared.

## THEORY

Previous implementations of CS to multidimensional SI have been formulated based on the signal equation for a single channel. Multicoil scans were reconstructed channel by channel and combined as a sum-of-squares (13,14). This single-channel problem is formulated as a minimization of an $\ell_1$-norm term while maintaining data consistency through an $\ell_2$-norm term and can be written as

$$\min_u ||\phi(u)||_1 \quad \text{s.t.} \quad ||R\mathcal{F}u - f||_2^2 < \sigma^2 \qquad [1]$$

where $u = u(x, y, z, F_2, F_1)$ is the reconstructed data, $f = f(k_x, k_y, k_z, t_2, t_1)$ is the undersampled data, $\sigma^2$ is an estimate of the noise variance of the sampled data, $R$ is the sampling mask, $\mathcal{F}$ is the Fourier transform, and $\phi(u)$ is a function that transforms $u$ to a sparse domain. The simplest choice is the identity transform $\phi(u) = u$, which is applicable only when the reconstructed data are self sparse. Alternatively, $\phi$ can be a wavelet transform or a combination finite difference operator as in total variation $\phi(u) = TV(u)$.

Unlike conventional $\ell_1$-norm-based CS reconstructions that consider each transform coefficient independently, GS (15) exploits the tendency of large transform coefficients to be clustered. In order to do this, certain coefficients are grouped and reconstructed as a unit. This grouping allows points in a group to influence each other as a model of signal correlation and has been shown to offer improved results compared to $\ell_1$ minimization in the context of MR (16–18).

### Single Channel GS Reconstruction

The objective of a GS reconstruction problem is an $\ell_{2,1}$ mixed-norm in which the $\ell_1$-norm of the $\ell_2$-norms of each group is minimized.

$$||Gu||_{2,1} = \sum_i^n ||u_{g_i}||_2 \qquad [2]$$

where $G \in \mathrm{R}^{n \times N}$ is the matrix operator that places $N$ vectorized points of $u$ into $n$ different groups. There is a lot of freedom in the choice of grouping. Groups can be identically sized or varying, and they can partition the entire region or overlap with each other.

In (18), the single channel GS problem

$$\min_u ||Gu||_{2,1} \quad \text{s.t.} \quad ||R\mathcal{F}u - f||_2^2 < \sigma^2 \qquad [3]$$

was solved using the split Bregman algorithm [19], and similarly in (20), it was solved using the alternate direction method of multipliers (ADMM).

### Multichannel GS Reconstruction

The multicoil CS problem can easily be formulated as a regularized SENSE (21) reconstruction (22,23). If the coil sensitivity profiles $S$ are known, the multicoil GS problem is

$$\min_u ||Gu||_{2,1} \quad \text{s.t.} \quad ||R\mathcal{F}Su - f||_2^2 < \sigma^2 \qquad [4]$$

While Eq. [4] closely resembles Eq. [3], $S$ prevents direct solutions using either split Bregman or ADMM. Both methods achieve their high efficiency because the most expensive subproblem involves inverting a circulant matrix with a Fourier transform to diagonalize it. But once $S$ is included, the matrix that must be inverted ($\mu S'\mathcal{F}'R'R\mathcal{F}S + \lambda G'G$) is no longer circulant. A few iterations of the conjugate gradient method can be used to approximate the noncirculant matrix inversion, but this can be expensive even with preconditioning (19,24). Alternatively, variable splitting can be applied to the data fidelity term in the same way it is applied to the objective term at the expense of an additional parameter and without the same guarantees of convergence (25,26).

The reconstructed data, $u$, must be self-sparse since the problem seeks to minimize the $\ell_{2,1}$-norm of groups with no additional transform. Therefore, individual coil data $Su$ must also be self-sparse. Instead of Eq. [4], the SENSE-regularized multicoil GS problem can be formulated as

$$\min_u ||GSu||_{2,1} \quad \text{s.t.} \quad ||R\mathcal{F}Su - f||_2^2 < \sigma^2 \qquad [5]$$

This problem is actually easier to solve than Eq. [4] as it requires one less auxiliary variable to be iteratively updated. Applying the substitution $v = Su$, gives

$$\min_{u,v} ||Gv||_{2,1} \quad \text{s.t.} \quad ||R\mathcal{F}v - f||_2^2 < \sigma^2, \quad v = Su \qquad [6]$$

where $v = v(x, y, z, F_2, F_1, c)$ is a 6D matrix with the inclusion of the channel dimension $c$. Since $u$ has been completely decoupled from the rest of the optimization, the problem can be solved iteratively for $v$ first before transforming back to $u$.

Ignoring the $v = Su$ constraint, the remaining problem is simply the single-channel GS formulation in Eq. [3] with $v$ replacing $u$. It is solved exactly as before by relaxing the constraint, making the substitution $z = Gv$, using the Bregman formulation, and iteratively solving each subproblem while holding the other variable constant. Bregman updates are applied, including over an outer loop on $f$ until the problem is accurately solved for $v$. The intermediate solution $v$ is practically equivalent to the reconstructed coil images that would be calculated individually in a channel-by-channel reconstruction except stacked as

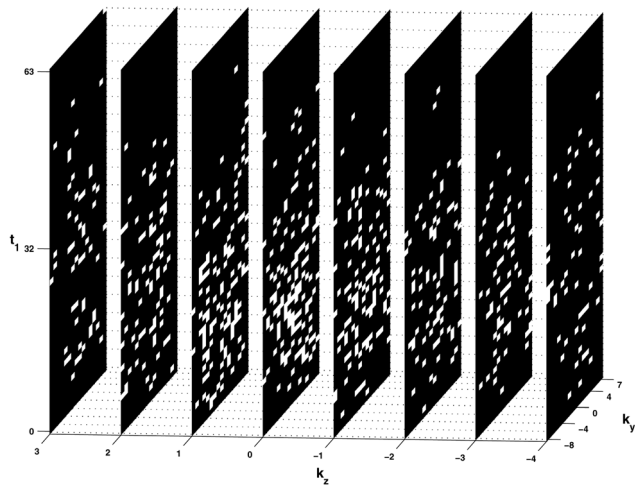


FIG. 1. 12× nonuniform sampling mask over the $(k_y, k_z, t_1)$ volume used to acquire accelerated EP-COSI data in multichannel acquisitions. White squares indicate sampled points. The mask follows the sampling density given in Eq. [9].

one large matrix, provided that the coils are each scaled to the same noise level.

Next, $u$ is calculated from $v$ and $S$ by

$$u = (S'S)^{-1}S'v \qquad [7]$$

For maximal SNR, the reconstructed data can be whitened in order to remove any noise correlations between coils

$$u = \left(S'\Psi^{-1}S\right)^{-1}S'\Psi^{-1}v \qquad [8]$$

where $\Psi$ is the noise correlation matrix between the coils described in detail in (21).

## METHODS

### Sequence

All scans were acquired on a Siemens 3T Trio scanner. The fully sampled 5D (3 spatial + 2 spectral) EP-COSI sequence contained a k-space volume with 16 points in the readout direction ($k_x$) and 16 and 8 points in the two phase-encoding directions ($k_y$ and $k_z$, respectively). The field of view (FOV) was $16 \times 16 \times 12$ cm$^3$. Each $k_x$ line was repeatedly acquired for 256 complex $t_2$ points per TR, and 64 $t_1$ points [echo time increments] were acquired. The $(k_y, k_z, t_1)$ volume was prospectively nonuniformly undersampled by a factor of 8, 12, or 16 as described in the following section. The bandwidths in the direct ($F_2$) and indirect ($F_1$) spectral dimensions were 1190 and 1250 Hz, respectively. The 8× and 12× undersampled scans were acquired with TR/minimum TE = 1200/30 ms for scan times of 20 and 14 min, respectively. The 16× undersampled scans were acquired with TR/minimum TE = 1500/30 ms for a scan time of 13 min. Global water suppression was applied (27). Scans were acquired on a single channel transmit/receive extremity coil with 8× and 12× undersampling and on a 15-channel knee coil with 12× undersampling. A separate scan with full spatial sampling and a single TE was acquired without water suppression before each EP-COSI scan for reference to determine the complex coil sensitivities and took 2 min 28 s with TR = 1200 ms and 3 min 18 s with TR = 1500 ms. When time permitted, a fully sampled, single-slice multiecho EP-COSI (MEEP-COSI) (28) scan was also acquired through the central slice of the 3D volume with slice thickness of 2 cm. The rest of the applicable parameters were the same, and the single-slice scan took 13 min with TR = 1.5 s or 10 min with TR = 1.2 s. A fully sampled 5D EP-COSI phantom scan of a 500-mL corn oil flask was acquired and retrospectively undersampled for comparison.

### Apodization and NUS Masks

In an in vivo COSY spectrum, the cross-peak signal is up to an order of magnitude lower than the diagonal peaks. As the cross peaks are the most interesting and descriptive signals, apodization is applied in $t_2$ and $t_1$ to enhance them. The filters used were squared sine bells in each dimension, and they were applied before reconstruction to enhance the coherence transfer signal envelope. The unapodized data has much higher diagonal peak to cross peak dynamic range, and reconstruction would therefore favor the diagonal peaks at the expense of cross peaks. Post reconstruction apodization would not be able to restore the cross peaks once the minimization of the $\ell_{2,1}$-norm has effectively denoised them.

Incoherent aliasing was achieved by randomly undersampling the $(k_y, k_z, t_1)$ volume. In Ref. 14, the nonuniform sampling density followed a decaying exponential so that the highest SNR data points were adequately sampled. Here, we follow the same philosophy except that we wish to ensure the highest SNR data points after apodization were subsampled. For that reason, the sampling density function was given by

$$\rho(k_y, k_z, t_1) = \exp\left\{-\frac{|k_y|}{n_y} - \frac{|k_z|}{n_z}\right\} \cdot \sin^2\left\{\left(\frac{t_1}{n_1}\right)^{sk}\pi\right\} \qquad [9]$$

where $\rho(k_y, k_z, t_1)$ is the probability of sampling point $(k_y, k_z, t_1)$, $sk = 0.5$ is the skew parameter, and $n_y$, $n_z$, and $n_1$ give the number of points in the $y$, $z$, and $t_1$ dimensions, respectively. The skewed squared sine bell density function approximates the combined effect of squared sine bell apodization on a decaying exponential curve. The 12× nonuniform undersampling mask used in multichannel acquisition is shown in Figure 1; the 8× and 16× nonuniform undersampling masks used in single-channel acquisitions are shown in Supporting Information Figure S1.

### Reconstruction

The coil sensitivities $S$ were determined from the non water-suppressed reference scan by taking the first time point and dividing each channel by the sum-of-squares from all channels in order to determine the proportional contribution of each channel. This ensures that the product $S'S$ in Eq. [7] is invertible. The first time point was chosen because each resonance is in phase at the echo time. This is in contrast to methods that deconvolve the

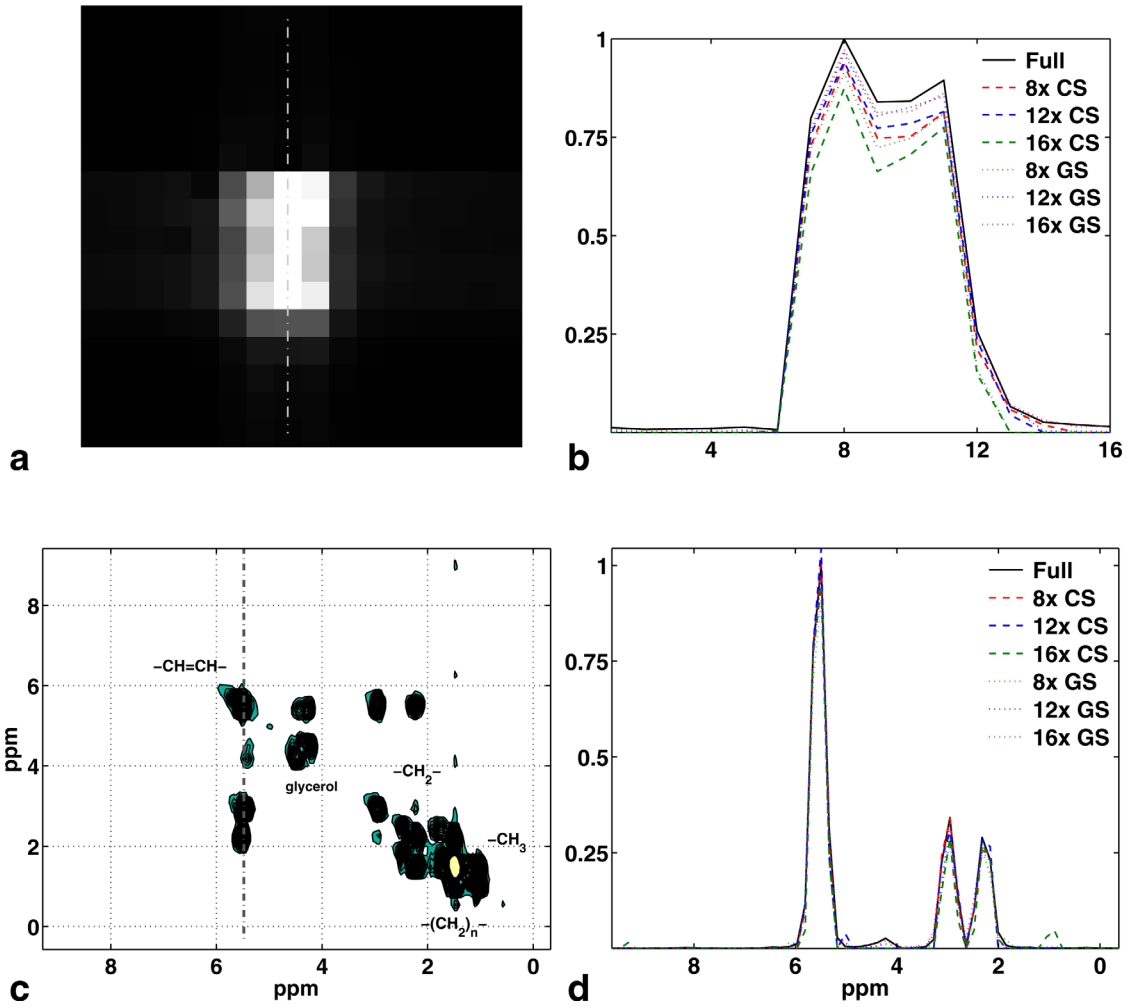


FIG. 2. (a) Metabolite map of the olefinic diagonal peak from a central slice of the fully sampled oil phantom scan. (b) Projection through the slice in (a) for each reconstruction. (c) COSY spectrum from a central voxel of the fully sampled data. (d) Projection through the COSY spectrum at $F_2 = 5.5$ ppm for each reconstruction.

phase at each time point that are applicable only when a single, large- signal solvent is present (29,30). A region of interest was also estimated from the reference sum-of-squares image where the intensities were greater than twice the mean.

As the $v$ optimization in Eq. [6] is equivalent to the $u$ optimization in Eq. [3], it can similarly be solved for the entire $v$ matrix at once or channel-by-channel. Here, Eq. [6] is solved channel-by-channel to reduce the dimensionality of the problem and allow for parallelization of the individual channel optimizations. If $v$ is solved as a 6D matrix at once, each channel should first be scaled to the same noise level so that a single value of $\sigma$ is appropriate for the entire dataset. If channels are not properly scaled, the reconstruction will be closest to the highest intensity coil regardless of its SNR, whereas a proper reconstruction should favor the highest SNR coils at each point. The noise in each coil can be determined from the standard deviation over a signal-free and artifact-free region of the spectrum. Here, we have used the region in ($F_2$, $F_1$) from (0,7) to (2,9) ppm.

Coefficients were grouped in the spectral plane ($F_2$, $F_1$) with 50% overlap between adjacent groups in each direction and with each group consisting of 8 × 4 points (18). This grouping strategy is motivated by the sparsity of the 2D COSY spectra-dominated by the presence of large peaks and is illustrated in Supporting Information Figure S2.

For comparison, undersampled data were also reconstructed with a self-sparse SENSE-based $\ell_1$-norm minimization

$$\min_u ||Su||_1 \quad \text{s.t.} \quad ||R\mathcal{F}Su - f||_2^2 < \sigma^2 \qquad [10]$$

This problem was also solved with the split Bregman algorithm using similar auxiliary variable substitutions as in Eq. [5]. The regularization parameters were set to $\mu = 1$ for both algorithms, $\lambda = 1/2$ for the CS problem, and $\lambda = 1/(2 \cdot 32)$ for the GS problem, where $\mu$ is the parameter that relaxes the data consistency constraint and $\lambda$ is the paramater that relaxes the variable substitution constraint. The solution from the split Bregman algorithm is relatively insensitive to these parameter choices (19), but the time to convergence can vary. The CS problem had a maximum of 100 outer Bregman iterations, the GS problem had a maximum of 50 outer

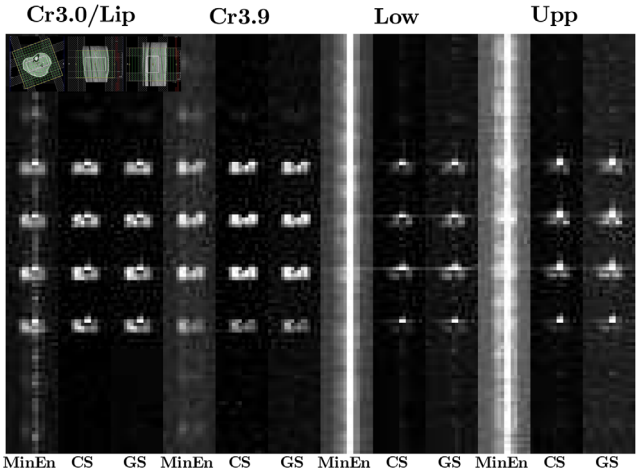


FIG. 3. Metabolite maps and localization from an 8× undersampled scan of the calf of a diabetic patient. Shown are the maps from the creatine and fat peak at 3.0 ppm (Cr3.0), the creatine resonance at 3.9 ppm (Cr3.9), and the lower (Low) and upper (Upp) IMCL and EMCL lipid cross peaks. Slices are stacked vertically, and the readout direction is horizontal. Within each metabolite group, the minimum energy reconstruction (MinEn) is shown with the CS and GS reconstructions, respectively. MinEn is scaled by the square root of the undersampling factor. Each metabolite is normalized to roughly the same gray scale.

iterations, and each problem had 15 inner Bregman iterations per outer iteration. The reconstructions were performed on a 64-bit octa core 3.1 GHz Intel Xeon E5-2687W processor with 128 GB RAM.

### Coil Compression

Whether the multichannel data are reconstructed coil-by-coil or as one large matrix, the reconstruction time is longer than for a single coil. In order to reduce the dimensionality of the problem and speed up the reconstruction, the 15-channel coil array was compressed into five virtual coils using a custom hybrid method based on (31) and (32). Since we already require explicit coil sensitivity maps and have a fully sampled spatial dimension, our method basically uses the transformation described by Buehrer *et. al.* (31) with an $A$ weighting matrix that is $x$-dependent

$$f(x)_k^{'} = A(x)f(x)_k \qquad [11]$$

where $f(x)_k$ are the $k$ data points at a given $x$ location in the original basis, and $f(x)_k^{'}$ is in the virtual coil basis. Original and transformed sensitivity maps are shown in Supporting Information Figure S3.

## RESULTS

A retrospectively undersampled phantom scan is shown in Figure 2. A vertical projection through the central slice is shown for each reconstruction and indicates that there is the expected loss in signal intensity for higher undersampling factors but that there is negligible difference in spatial resolution between the reconstructions and the fully sampled data. From the projection along the $F_1$ dimension, it is similarly shown that the spectral resolution remains constant as well, though some residual aliasing artifact can be seen with the 16× CS reconstruction around 1 ppm.

Figure 3 shows the 3D localization and metabolite maps from an 8× undersampled scan of the calf of a 57-year-old diabetic patient taken with a single channel extremity coil. Metabolite maps were computed by integrating over the regions around the creatine/lipid peak at 3.0 ppm, the creatine peak(s) at 3.9 ppm, the lower EMCL and IMCL cross peaks, and the upper cross peaks, respectively. Within each metabolite grouping, the minimum energy reconstruction (missing data points filled in with zeros), the CS reconstruction (using Eq. [10]), and the GS reconstruction (using Eq. [5]) are shown. The minimum energy reconstruction is scaled by the square root of the undersampling factor to produce similar intensities to the other reconstructions. Note the aliasing in both phase-encoding directions in the minimum energy reconstruction. The CS and GS maps look very similar, with the GS maps appearing slightly noisier.

Figure 4 shows COSY spectra from the tibial bone marrow and the soleus and tibialis anterior muscles. From the full COSY spectra, the $t_1$ aliasing is apparent. The CS reconstructions provide good denoising and remove the aliasing of many of the peaks, but the aliasing due to the two dominant lipid peaks and residual water remains. This aliasing nearly completely obscures the lower EMCL/IMCL cross peaks, as only the GS reconstruction faithfully shows the splitting of the EMCL and IMCL components in the lower cross peaks in both the soleus and tibialis anterior that are found in diabetic patients.

Each reconstruction faithfully reconstructs the spatial locations as can be seen by looking at the spectrum around the 3.9 ppm diagonal, as creatine is absent in the marrow, a strong singlet in the soleus, and a split doublet in the tibialis anterior (33). For the reconstructions shown in Figures 3 and 4, the GS converged after only five outer iterations in about 15 minutes, while the CS reconstruction did not fully converge in 100 outer iterations and took almost an hour. The minimum energy spectra from these locations are shown in Supporting Information Figure S4.

Figures 5 and 6 show metabolite maps and full spectra from a 16× prospectively undersampled scan of the same 57-year-old diabetic adult taken on a different day than the 8× scan. Aliasing is even more prevalent with the higher undersampling factors. Again, GS reconstruction appears slightly noisier but has a much greater reduction in aliasing compared to CS. In all cases, the spectra are not quite as clean as the 8× undersampled, with some smaller peaks and the separation between EMCL and IMCL being difficult to resolve. Here, GS converged after 16 outer iterations in about 45 min, while CS again took 100 outer iterations and just under an hour.

Contour plots of the creatine signal at 3.9 ppm are shown for single-slice MEEP-COSI in Figure 7b and the three central slices of a 12× undersampled 5D EP-COSI in Figure 7c–e in a healthy 34-year-old calf. The MEEP-COSI reconstruction used all 15 acquired channels,

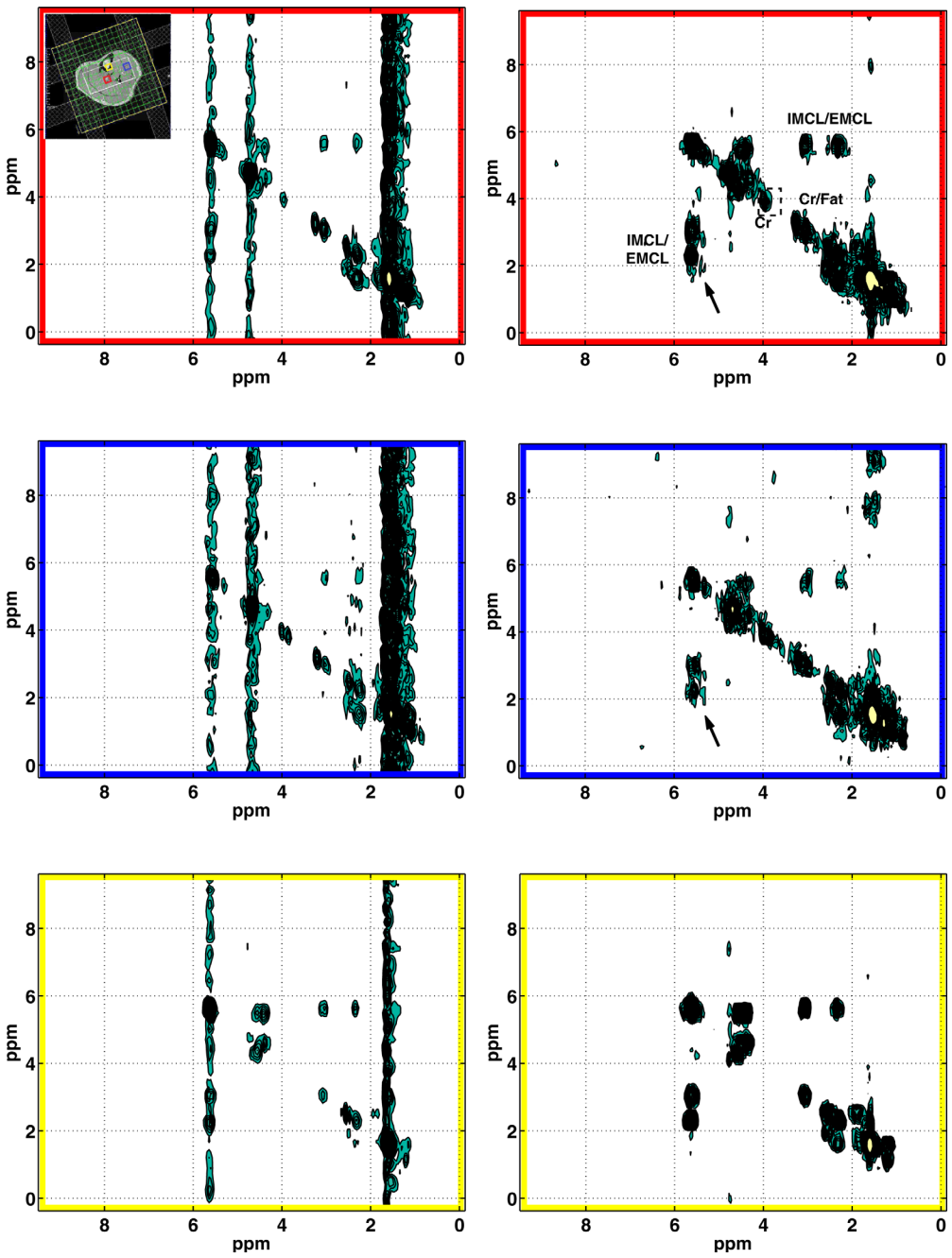


FIG. 4. COSY spectra from the highlighted voxels in a central slice (insert) of the same scan as Figure 3. CS-reconstructed spectra are shown on the left, while GS-reconstructed are shown on the right. The red voxels are from the soleus muscle, blue are from the tibialis anterior muscle, and yellow are from the marrow. Arrows highlight the splitting of the IMCL and EMCL cross peaks in both the soleus and tibialis anterior seen in diabetic patients. Contour levels are the same for each reconstruction for a given voxel.

while the 5D EP-COSI reconstruction used only the first five virtual channels. The CS reconstruction took an average of 73 iterations and 47 min per coil (almost 4 h total), and the GS reconstruction took an average of 15 iterations and 54 min per coil (about 4.5 h total). Each shows similar localization with the single, strong peak in the soleus, a split doublet in the tibialis anterior, and little creatine signal in the marrow. The MEEP-COSI scan has somewhat higher SNR and a cleaner profile, but the thinner slices of the 5D EP-COSI better show the location of the fibular marrow at the bottom right of the volume of interest and the doublet splitting in the gastrocnemius at the bottom left.

## DISCUSSION

Comparing the contour plots in Figure 7 suggests that reconstructed data have some residual in plane signal bleed compared to the fully sampled single slice. This is likely due to the small amount of blurring caused by reconstruction, as it is also seen slightly in the indirect spectral dimension. It may also be due to some residual

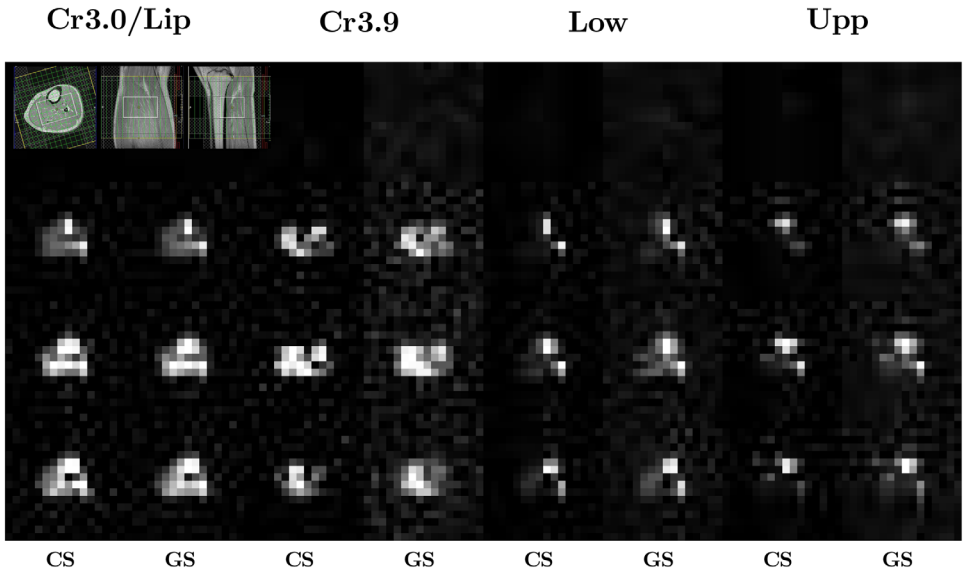


FIG. 5. Metabolite maps over the central four slices from a 16× undersampled scan. The top slice was outside the VOI and has no signal. Shown are the maps from the creatine and fat peak at 3.0 ppm (Cr3.0), the creatine resonance at 3.9 ppm (Cr3.9), and the lower (Lower) and upper (Upper) IMCL and EMCL lipid cross peaks. Slices are stacked vertically, and the readout direction is horizontal. For each metabolite group, the CS reconstruction is shown on the left, and GS reconstruction is shown on the right.

aliasing, but the COSY spectra in Figures 4 and 6 suggest that spectral aliasing is removed by the GS reconstruction.

Although the additional computation of grouping and taking the $\ell_2$-norm over each group prolongs each iteration of GS, the algorithm converged for each dataset and did so with far fewer iterations than CS. This is because the $\ell_{2,1}$ mixed-norm regularizer promotes global sparsity while allowing local curvature and is therefore a much better model for in vivo COSY spectra compared to the $\ell_1$-norm regularizer which promotes sparsity both locally and globally. This allows the algorithm to take larger steps toward convergence.

The number of outer iterations in the CS problem was chosen such that most reconstructions would converge or be close to convergence and that each coil reconstruction would take under an hour. Nevertheless, when the number of outer iterations was not restricted, some of the CS reconstructions took much longer before finally converging, yet visual inspection of the data did not show much, if any, improvement beyond the first 100 iterations. Therefore, the limit of 100 outer iterations is justified and is already more than in previous implementations (14,18). With those limits, each method seems to take about 45–55 min per coil, though some are significantly shorter. We have favored using constant values of the regularization parameters for ease of implementation and reproducibility, but a more adaptive choice could affect the convergence rates of the algorithms and the total reconstruction time. Choice of regularization parameters is an active area of research in CS (34,35).

It is well known that SENSE acceleration comes with an added SNR expense known as the *g*-factor (21), while CS reconstruction offers SNR enhancement (36). That is one reason why these techniques are so complementary, but it also means there is ambiguity in how the reconstructed SNR compares to the true SNR of fully sampled data. For instance, the reconstructed SNR is dependent moreso on the parameter $\sigma$ than on the acquired data and is not a good measure of data quality on its own. Therefore, it is best to use a conservative estimate of $\sigma$ that favors data fidelity to prevent the reconstruction from becoming overly denoised. In such cases, the quality of the reconstructed data is dependent on the SNR of the acquired data (which is typically high for COSY spectra in skeletal muscle) and the magnitude of the artifacts (which depends on the degree of undersampling). This article shows that the GS reconstruction performs better than conventional CS reconstruction when the undersampling artifacts are large. It is expected that similar results would be obtained for inherently low SNR acquisitions.

Previous work with 3D volumetric J-resolved SI suggests that minimizing the TV performs somewhat better than the CS reconstruction presented here (14). The difference was not overwhelming, though, and work with single-slice localized EP-COSI shows GS performing much better than either CS or TV (18). Incorporating a third spatial dimension increases the self-sparsity of the data relative to single slice, so this suggests that applying a sparsifying transform, such as TV, to the 3D-COSI problem would not yield significantly better results than GS. Including grouping with a TV regularizer could offer improved performance and is an area of active research.

The methods presented here used Fourier encoding for all three spatial dimensions. As in (14), this allows us to undersample across the entire $(k_y, k_z, t_1)$ volume. Undersampling across higher-dimensional space produces more incoherent artifacts and is a requisite for the large acceleration factors presented here. Alternatively, 3D spatial encoding can also be achieved using a multislice acquisition with Fourier encoding in the other spatial dimensions. In that case, each slice could be undersampled differently in $(k_y, t_1)$, enhancing the incoherence compared to a single slice but not producing the incoherence of the 3D Fourier method (37). In Hadamard encoding, each slice is encoded simultaneously, so there is no incoherence enhancement due to the slice dimension.

In the reconstruction method applied here, grouping was done across the two dimensions of the spectral plane as in (18) to take advantage of the bunching of large coefficients in a highly sparse COSY spectrum.

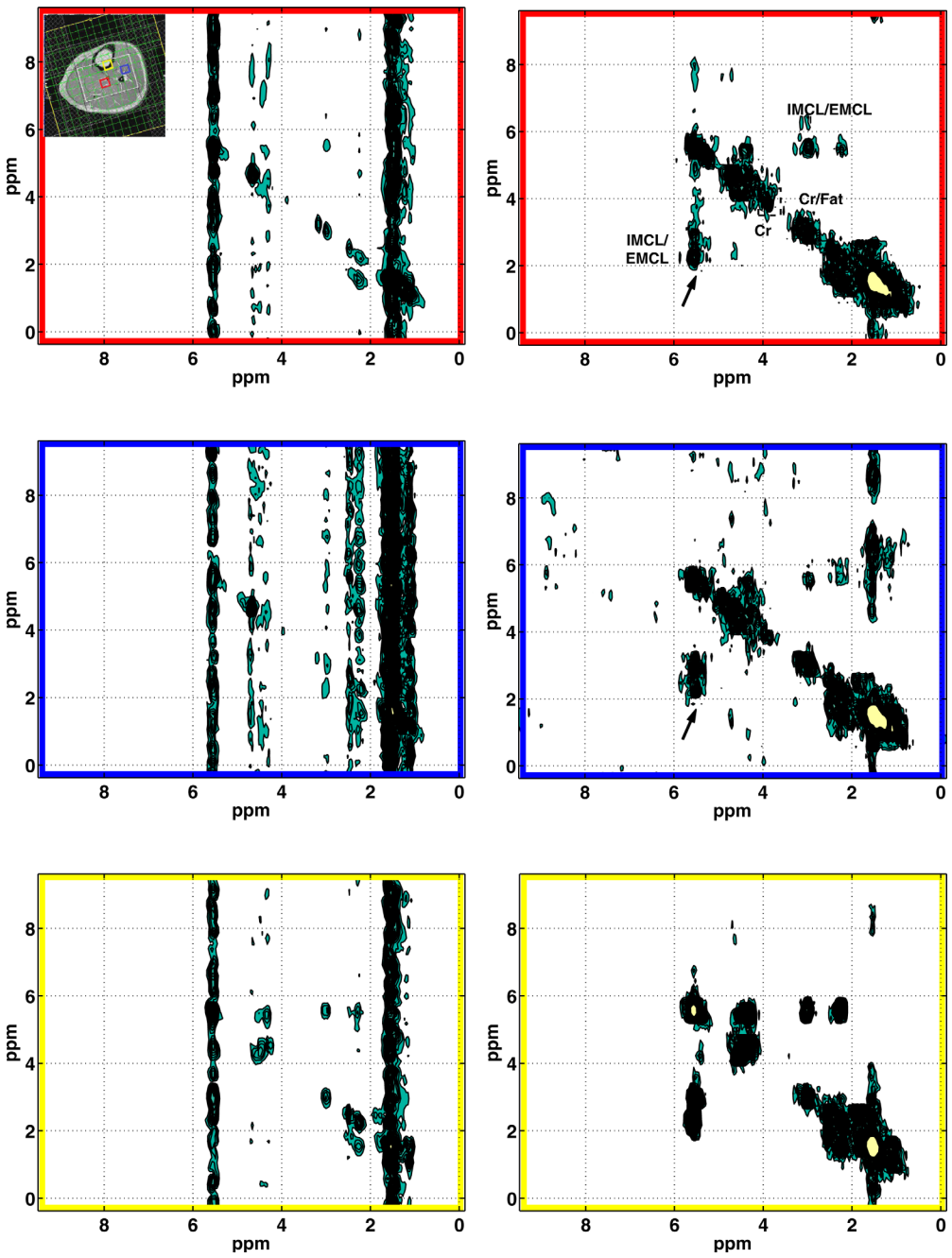


FIG. 6. COSY spectra from the highlighted voxels in a central slice (insert) of the same scan as Figure 5. CS-reconstructed spectra are on the left, GS-reconstructed are shown on the right. Red voxels are from the soleus muscle, blue are from the tibialis anterior muscle, and yellow are from the marrow. The splitting of the IMCL and EMCL cross peaks in the soleus and tibialis anterior is indicated. Contour levels are the same for each reconstruction for a given voxel.

However, grouping does not need to be restricted to the spectral plane and could take advantage of the proximity of large coefficients in the spatial dimensions as well. The algorithm simply requires the number of points in each group to be the same. Joint sparsity is a form of group sparsity in which grouping is done over the coil dimension and could also be applied here (38,39), except in that case, the ability to reconstruct channels individually is precluded. Mild improvement in reconstruction quality has been shown using joint sparsity compared to channel-by-channel reconstructions (40,41).

The EP-COSI and MEEP-COSI sequences both used a PRESS volumetric slice selection module in which each of the three pulses selects an orthogonal slice (42), and the intersection of the slices is the VOI. This method results in a clean, box-like profile in each dimension and lends itself to region of interest definition in the coil compression matrix of Eq. [11]. A shorter version of the sequence similar to the original COSY can be constructed using two 90° pulses that select a single slice only. The two-pulse sequence would have a shorter minimum echo time and reduced SAR, but excitation cannot be limited

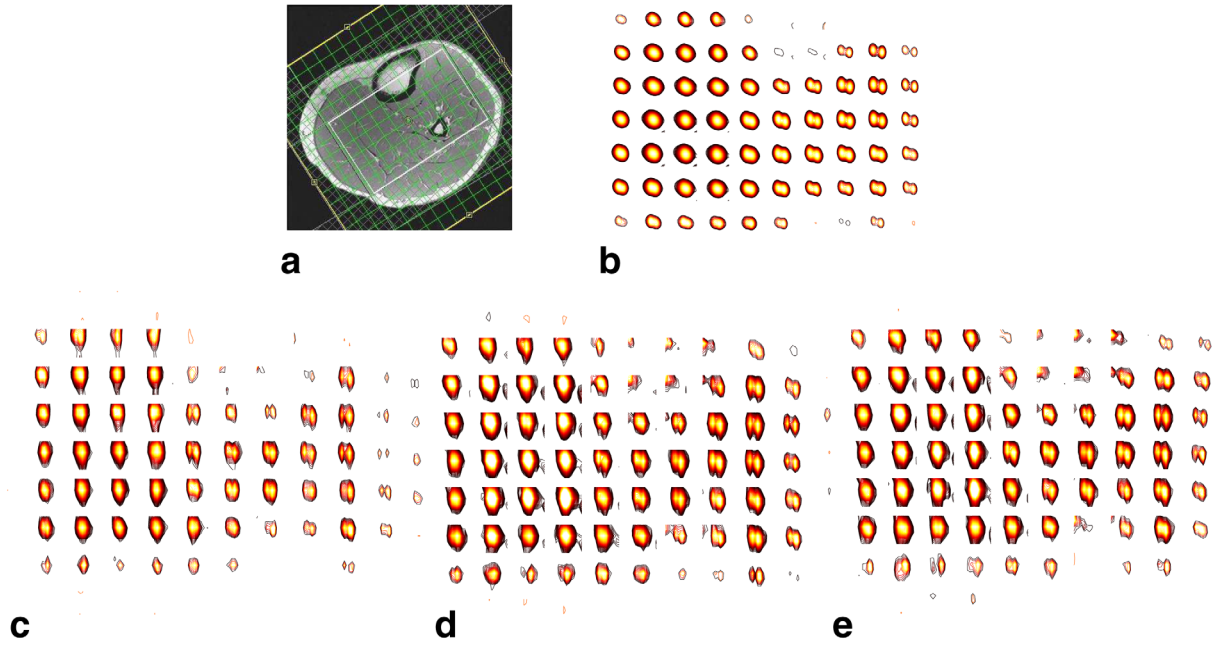


FIG. 7. Axial localization with 15-channel knee coil (a). Contour plot of the distribution of the peaks at 3.9 ppm for a single slice MEEP-COSI scan (b) and the central three slices from 12× undersampled 5D EP-COSI (c-e) in the same healthy volunteer. The undersampled 5D EP-COSI scan took 14 min, and the MEEP-COSI scan took 13 min.

to a VOI. Even using PRESS localization, a small amount of the marrow was included. Although the calf muscles have a large of amount of lipid signal, the marrow has more, which results in signal bleed as seen in Figures 3 and 5. Also, many muscle spectroscopy studies look at overweight and obese patients whose calves often have a large amount of subcutaneous EMCL. Unlike techniques in slice-based SI in brain that use inversion recovery to selectively suppress the lipid signal (43), the lipid signal is often of primary interest in the muscle, and it has been shown that the IMCL peak has longer T2 and is better resolved at long TE (44). Outer volume suppression is an alternative that can be used to ensure proper VOI excitation (45) but is limited by the number of saturation bands that can be applied.

## CONCLUSION

A 5D correlated SI sequence with echo planar readout is presented here that is achievable only by highly undersampling the volume of the two phase-encoding dimensions and one indirect spectral dimension. Reconstruction of the data using group sparsity minimizes the mixed $\ell_{2,1}$-norm of the data and takes advantage of the proximity of high amplitude coefficients found in spectroscopy peaks. Group sparsity reconstructs much better than a standard $\ell_1$-norm minimization algorithm without significant time penalty.

## REFERENCES

1. Aue WP, Bartholdi E, Ernst RR. Two-dimensional spectroscopy. Application to nuclear magnetic resonance. J Chem Phys 1976;64: 2229–2246.
2. Brereton IM, Galloway GJ, Rose SE, Doddrell DM. Localized two-dimensional shift correlated spectroscopy in humans at 2 Tesla. Magn Reson Med 1994;32:i251–257.
3. Thomas MA, Yue K, Binesh N, et al. Localized two-dimensional shift correlated MR spectroscopy of human brain. Magn Reson Med 2001; 46:58–67.
4. Velan SS, Durst C, Lemieux SK, Raylman RR, Sridhar R, Spencer RG, Hobbs GR, Thomas MA. Investigation of muscle lipid metabolism by localized one- and two-dimensional MRS techniques using a clinical 3T MRI/MRS scanner. J Magn Reson Imaging 2007;25:192–199.
5. Brown TR, Kincaid BM, Ugurbil K. NMR chemical shift imaging in three dimensions. Proc Natl Acad Sci 1982;79:3523–3526.
6. Ziegler A, Metzler A, Kckenberger W, Izquierdo M, Komor E, Haase A, Dcorps M, von Kienlin M. Correlation-Peak Imaging. J Magn Reson Ser B 1996;112:141–150.
7. Mansfield P. Spatial mapping of the chemical shift in NMR. Magn Reson Med 1984;1:370–386.
8. Posse S, DeCarli C, Le Bihan D. Three-dimensional echo-planar MR spectroscopic imaging at short echo times in the human brain. Radiology 1994;192:733–738.PMID: 8058941.
9. Mayer D, Dreher W, Leibfritz D. Fast echo planar based correlation-peak imaging: Demonstration on the rat brain in vivo. Magn Reson Med 2000;44:23–28.
10. Lipnick S, Verma G, Ramadan S, Furuyama J, Thomas MA. Echo planar correlated spectroscopic imaging: Implementation and pilot evaluation in human calf in vivo. Magn Reson Med 2010;64:947–956.
11. Andronesi OC, Gagoski BA, Adalsteinsson E, Sorensen AG. Correlation chemical shift imaging with low-power adiabatic pulses and constant-density spiral trajectories. NMR Biomed 2012;25:195–209.
12. Burns B, Wilson NE, Furuyama JK, Thomas MA. Non-uniformly under-sampled multi-dimensional spectroscopic imaging in vivo: Maximum entropy versus compressed sensing reconstruction. NMR Biomed 2014;27:191–201.
13. Furuyama JK, Wilson NE, Burns BL, Nagarajan R, Margolis DJ, Thomas MA. Application of compressed sensing to multidimensional spectroscopic imaging in human prostate. Magn Reson Med 2012;67: 1499–1505.
14. Wilson NE, Iqbal Z, Burns BL, Keller M, Thomas MA. Accelerated five-dimensional echo planar J-resolved spectroscopic imaging: Implementation and pilot validation in human brain. Magn Reson Med, in press. doi is 10.1002/mrm.25605
15. Yuan M, Lin Y. Model selection and estimation in regression with grouped variables. J R Stat Soc Ser B 2006;68:49–67.
16. Usman M, Prieto C, Schaeffter T, Batchelor PG. kt group sparse: A method for accelerating dynamic MRI. Magn Reson Med 2011;66: 1163–1176.

17. Prieto C, Usman M, Wild JM, Kozerke S, Batchelor PG, Schaeffter T. Group sparse reconstruction using intensity-based clustering. Magn Reson Med 2013;69:1169–1179.
18. Burns BL, Wilson NE, Thomas MA. Group Sparse Reconstruction of Multi-Dimensional Spectroscopic Imaging in Human Brain in vivo. Algorithms 2014;7:276–294.
19. Goldstein T, Osher S. The split Bregman method for L1 regularized problems. SIAM J Imaging Sci 2009;2:323–343.
20. Deng W, Yin W, Zhang Y. Group sparse optimization by alternating direction method. In Proceedings of SPIE, San Diego, CA, vol. 8858, 2013. pp. 88580R–88580R–15. doi:10.1117/12.2024410.
21. Pruessmann KP, Weiger M, Scheidegger MB, Boesiger P. SENSE: Sensitivity encoding for fast MRI. Magn Reson Med 1999;42:952–962.
22. Block KT, Uecker M, Frahm J. Undersampled radial MRI with multiple coils. Iterative image reconstruction using a total variation constraint. Magn Reson Med 2007;57:1086–1098.
23. Liang D, Liu B, Wang J, Ying L. Accelerating SENSE using compressed sensing. Magn Reson Med 2009;62:1574–1584.
24. Compton R, Osher S, Bouchard L. Hybrid regularization for MRI reconstruction with static field inhomogeneity correction. In 2012 9th IEEE International Symposium on Biomedical Imaging (ISBI), Barcelona, 2012. pp. 650–655.
25. Ramani S, Fessler J. Parallel MR image reconstruction using augmented Lagrangian methods. IEEE Trans Med Imaging 2011;30:694–706.
26. Chen Y, Hager W, Huang F, Phan D, Ye X, Yin W. Fast algorithms for image reconstruction with application to partially parallel MR imaging. SIAM J Imaging Sci 2012;5:90–118.
27. Ogg R, Kingsley R, Taylor J. WET, a T1- and B1-insensitive water-suppression method for in vivo localized 1H NMR spectroscopy. J Magn Reson Ser B 1994;104:1–10.
28. Furuyama JK, Nagarajan R, Roberts CK, Lee CC, Hahn TJ, Thomas MA. A pilot validation of multi-echo based echo-planar correlated spectroscopic imaging in human calf muscles. NMR Biomed 2014;27:1176–1183.
29. Klose U. In vivo proton spectroscopy in presence of eddy currents. Magn Reson Med 1990;14:26–30.
30. Roebuck JR, Hearshen DO, O'Donnell M, Raidy T. Correction of phase effects produced by eddy currents in solvent suppressed 1H-CSI. Magn Reson Med 1993;30:277–282.
31. Buehrer M, Pruessmann KP, Boesiger P, Kozerke S. Array compression for MRI with large coil arrays. Magn Reson Med 2007;57:1131–1139.
32. Zhang T, Pauly JM, Vasanawala SS, Lustig M. Coil compression for accelerated imaging with Cartesian sampling. Magn Reson Med 2013;69:571–582.
33. Kreis R, Boesch C. Liquid-crystal-like structures of human muscle demonstrated by in vivo observation of direct dipolar coupling in localized proton magnetic resonance spectroscopy. J Magn Reson Ser B 1994;104:189–192.
34. Hansen PC, OLeary DP. The use of the L-curve in the regularization of discrete Ill-posed problems. SIAM J Sci Comput 1993;14:1487–1503.
35. Ramani S, Liu Z, Rosen J, Nielsen J, Fessler J. Regularization parameter selection for nonlinear iterative image restoration and MRI reconstruction using GCV and SURE-based methods. IEEE Trans Image Process 2012;21:3659–3672.
36. Rudin LI, Osher S, Fatemi E. Nonlinear total variation based noise removal algorithms. Phys D 1992;60:259 –268.
37. Lustig M, Donoho D, Pauly JM. Sparse MRI: The application of compressed sensing for rapid MR imaging. Magn Reson Med 2007;58:1182–1195.
38. Duarte M, Sarvotham S, Baron D, Wakin M, Baraniuk R. Distributed compressed sensing of jointly sparse signals. In Conference Record of the Thirty-Ninth Asilomar Conference on Signals, Systems and Computers, Asilomar, 2005 pp. 1537–1541.
39. Vasanawala S, Murphy M, Alley M, Lai P, Keutzer K, Pauly J, Lustig M. Practical parallel imaging compressed sensing MRI: Summary of two years of experience in accelerating body MRI of pediatric patients. In From Nano to Macro, 2011 IEEE International Symposium on Biomedical Imaging, Chicago. 2011, pp. 1039–1043.
40. Otazo R, Kim D, Axel L, Sodickson DK. Combination of compressed sensing and parallel imaging for highly accelerated first-pass cardiac perfusion MRI. Magn Reson Med 2010;64:767–776.
41. Akcakaya M, Hu P, Chuang ML, Hauser TH, Ngo LH, Manning WJ, Tarokh V, Nezafat R. Accelerated noncontrast-enhanced pulmonary vein MRA with distributed compressed sensing. J Magn Reson Imaging 2011;33:1248–1255.
42. Bottomley PA. Spatial localization in NMR spectroscopy in vivo. Ann N Y Acad Sci 1987;508:333–348.
43. Spielman DM, Pauly JM, Macovski A, Glover GH, Enzmann DR. Lipid-suppressed single-and multisection proton spectroscopic imaging of the human brain. J Magn Reson Imaging 1992;2:253–262.
44. Ren J, Sherry AD, Malloy CR. 1H MRS of intramyocellular lipids in soleus muscle at 7 T: Spectral simplification by using long echo times without water suppression. Magn Reson Med 2010;64:662–671.
45. Singh S, Rutt BK, Henkelman RM. Projection presaturation: a fast and accurate technique for multidimensional spatial localization. J Magn Reson 1990;87:i567–583.

## SUPPORTING INFORMATION

Additional Supporting Information may be found in the online version of this article.

**Supporting Figure S1:** 8x (a) and 16x (b) NUS masks over the (ky; kz; t1) volume used to acquire accelerated EP-COSI data in the single channel acquisitions. White squares indicate sampled points. Each mask follows the sampling density given in Eq. (9) in the manuscript.

**Supporting Figure S2:** Illustration of the dierence between two dimensional groups that are non-overlapping and those with 50% overlap. The overlapping groups were used to combine coecients in the spectral plane (F2, F1).

**Supporting Figure S3:** Magnitude of sensitivity maps from 15-channel data taken directly from a water reference scan (a), after using an x-dependent geometric transformation matrix A(x) (Eq. (11)) (b), and after coil compression using a single transformation matrix A (c). Maps were masked to the ROI.

**Supporting Figure S4:** Minimum energy reconstruction of voxels shown in Fig. 4 (top row) and 6 (bottom row). Contours are scaled by the square root of the undersampling factor to show similar signal magnitudes to the reconstructed data. Aliasing is prevalent in the F1 dimension in each case, regardless of the SNR.